




ARTICLE

<https://doi.org/10.1038/s42005-019-0196-7>

OPEN

# Microscopic observation of efficient charge transport processes across domain boundaries in donor-acceptor-type conjugated polymers

Hisaaki Tanaka <sup>1</sup>, Ayato Wakamatsu<sup>1</sup>, Masahiro Kondo<sup>1</sup>, Shinya Kawamura<sup>1</sup>, Shin-ichi Kuroda<sup>1,2</sup>, Yukihiko Shimoi<sup>3</sup>, Won-Tae Park <sup>4</sup>, Yong-Young Noh <sup>4,5</sup> & Taishi Takenobu<sup>1</sup>

Backbone rigidity of conjugated polymers is suggested to play an essential role in realizing high-mobility transistors through the efficient interconnection of crystalline domains by tie molecules as discussed for the recently-developed donor-acceptor (DA)-type copolymers. However, no studies have directly observed interdomain hopping in these DA copolymers. Here, highly-efficient interdomain charge transport is observed in two typical high-mobility DA copolymers from the microscopic observation of charge carriers using field-induced electron spin resonance (ESR) spectroscopy. The in-plane ESR signal exhibits a clear motional narrowing effect associated with the carrier motion across the boundaries. The activation energy of the interdomain charge motion is as low as that of intradomain motion (~10 meV), both of which are clearly lower than those observed in the conventional semicrystalline polymer. The structural origin of this efficient interdomain electrical connection is the rigid, nearly torsion-free backbone conformation of the tie molecule, as demonstrated from density functional theory calculations.

<sup>1</sup> Department of Applied Physics, Nagoya University, Chikusa, Nagoya 464-8603, Japan. <sup>2</sup> Toyota Physical and Chemical Research Institute (TPCRI), 41-1, Yokomichi, Nagakute, Aichi 480-1192, Japan. <sup>3</sup> Research Center for Computational Design of Advanced Functional Materials (CD-FMat), National Institute of Advanced Industrial Science and Technology (AIST), 1-1-1 Umezono, Tsukuba, Ibaraki 305-8568, Japan. <sup>4</sup> Department of Energy and Materials Engineering, Dongguk University, 30, Pildong-ro 1-gil, Jung-gu, Seoul 04620, Korea. <sup>5</sup> Department of Chemical Engineering, Pohang University of Science and Technology (POSTECH), 77 Cheongam-Ro, Nam-Gu, Pohang 37673, Republic of Korea. Correspondence and requests for materials should be addressed to H.T. (email: [htanaka@nuap.nagoya-u.ac.jp](mailto:htanaka@nuap.nagoya-u.ac.jp)) or to Y.-Y.N. (email: [yynoh@postech.ac.kr](mailto:yynoh@postech.ac.kr)) or to T.T. (email: [takenobu@nagoya-u.jp](mailto:takenobu@nagoya-u.jp))

Conjugated polymers have been extensively investigated as materials for low-cost, light-weight, and flexible electronic devices, such as thin-film transistors (TFTs). In general, charge transport in polymer thin films is highly susceptible to structural/energetic disorders, which are inevitably introduced into the films and/or device interfaces<sup>1–7</sup>. Thus, suppression of these disorders has been a major subject for improving the mobility of polymeric TFTs. From a materials perspective, the use of semicrystalline-conjugated polymers, such as poly(3-hexylthiophene) (P3HT) and poly(2,5-bis(3-alkylthiophene-2-yl)thieno[3,2-*b*]thiophene) (PBTTT, Fig. 1a), has been a major approach for this purpose<sup>8–11</sup>. In these materials, large crystalline domains with edge-on molecular orientations are formed within the film, as schematically illustrated in Fig. 1b. Nearly two-dimensional charge delocalization is expected within these crystallites through the  $\pi$ - $\pi$  stacking network, resulting in high TFT mobilities up to  $1 \text{ cm}^2 \text{ V}^{-1} \text{ s}^{-1}$  (refs. 10,12). However, even in these semicrystalline materials, positional disorders of the molecules within the crystallite are still non-negligible, producing charge trapping sites<sup>13,14</sup>. Furthermore, domain boundaries between adjacent crystallites, as well as amorphous regions surrounding the crystallites, can also be a major source of charge trapping, although the presence of tie molecules improves the electrical connectivity of the domains with different chain alignments within the film<sup>15–20</sup>.

In recent years, the emergence of another design principle of high-mobility materials has attracted considerable research interest<sup>21–23</sup>. Several groups of conjugated copolymers with donor–acceptor (DA)-type alternating backbones have exhibited surprisingly high mobilities exceeding  $1 \text{ cm}^2 \text{ V}^{-1} \text{ s}^{-1}$  without forming long-range ordered crystalline domains<sup>24–35</sup>. Even some of these polymers take face-on orientations and/or mixed edge-on and face-on orientations to the substrate, which are apparently disadvantageous for efficient charge transport through the transistor channel according to the above design principle for semicrystalline polymers. Through various structure–property studies, some key characteristics that enable charge transport that is resilient against structural disorders have been revealed for these DA copolymers. Among these characteristics, a rigid and nearly torsion-free backbone structure plays a crucial role in high mobilities; a long, highly planar polymer backbone without folding enables both nearly trap-free charge transport along the chain<sup>36–38</sup> and efficient interchain charge transfer through the strong  $\pi$ - $\pi$  interaction between adjacent D–A subunits<sup>23,24,36</sup>, thus improving the intrinsic charge transport within the ordered domains. In addition, this structural feature seems to be advantageous for interdomain transport through the efficient electrical connection of the domains by rigid tie molecules<sup>39</sup>. However, the above discussion is mostly based on the structural characterization or modeling of the polymer backbones and films<sup>21–23,36–38,40,41</sup>, and almost no direct observations of intradomain and interdomain charge transports have been reported in DA copolymers. To clarify the detailed charge transport mechanism and the complex structure–property relationship in DA copolymers, it is indispensable to understand the relationship between the microscopic structure and the carrier dynamics in these materials.

Field-induced electron spin resonance (FI-ESR) spectroscopy is a particularly suitable method for this purpose because it can sensitively detect charge carriers injected into the TFT devices, providing a variety of microscopic information which is crucial to understand the charge transport process at the insulator interface<sup>42–49</sup>. For example, local molecular orientation at the interface can be determined from the angular dependence of the *g* value. Furthermore, thermal carrier motion in thin films is directly reflected on the temperature dependence of the ESR linewidth and the line shape through the motional narrowing effect,

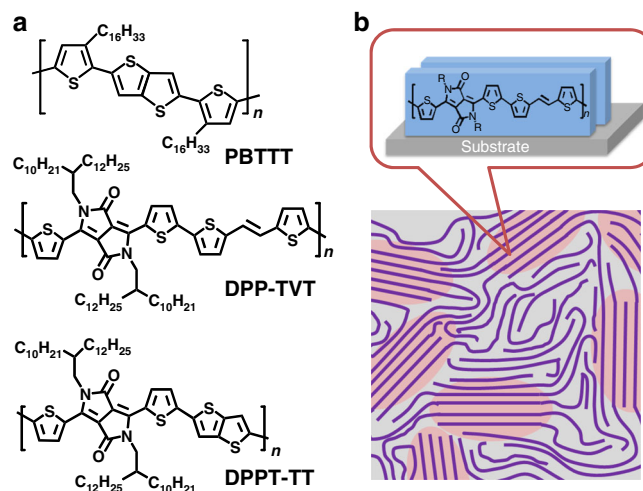


**Fig. 1** Chemical structures of target polymers and schematic illustration of the polymer film. **a** Chemical structures of poly(2,5-bis(3-alkylthiophene-2-yl)thieno[3,2-*b*]thiophene) (PBTTT) and diketopyrrolo-pyrrole (DPP)-based copolymers with a thiophene-vinylene-thiophene (TVT) unit (DPP-TVTV), and with thiophene (T)-thieno[3,2-*b*]thiophene (TT) unit (DPPT-TT). **b** Schematic illustration of the polymer thin films containing both crystalline (shaded areas) and amorphous regions. The molecules form ordered lamellar structures with an edge-on orientation on the substrate within the crystalline domains

providing a key to clarify the microscopic transport properties. Matsui et al.<sup>50</sup> have demonstrated that two types of motional narrowing effects are observed in polycrystalline thin films of PBTTT depending on the applied magnetic field directions, i.e., the narrowing due to the intradomain and interdomain carrier motions. In the case of uniaxially oriented molecules along the substrate normal, such as PBTTT in thin films, the former narrowing case is observed when the magnetic field (**H**) is perpendicular to the substrate ( $H_{\perp}$  configuration), whereas the latter case is observed when **H** is applied parallel to the substrate ( $H_{\parallel}$  configuration). In the case of PBTTT, the interdomain carrier hopping gives the same activation energy as that of the mobility, strongly indicating that the macroscopic charge transport is limited by domain boundaries in this system. Similar boundary-limited charge transport has also been reported for the TFTs of polycrystalline small molecules<sup>50,51</sup>. The direct evaluation of interdomain carrier motion similar to that described above can be a powerful method to confirm the interconnectivity of the domains in recently developed high-mobility DA copolymers.

In the present study, we demonstrate that diketopyrrolo-pyrrole (DPP)-based DA copolymers shown in Fig. 1a, with a thiophene-vinylene-thiophene (TVT) donor unit (DPP-TVTV)<sup>32,34,35</sup> and with thiophene (T)-thieno[3,2-*b*]thiophene (TT) donor units (DPPT-TT)<sup>28–31</sup>, indeed exhibit highly efficient charge carrier motions, as indicated by observing the temperature dependence of the FI-ESR linewidths. The former polymer takes a highly ordered lamellar structure, as in the case of semicrystalline polymers<sup>32</sup>, whereas the latter polymer takes less crystalline structures if the film is treated below  $150 \text{ }^{\circ}\text{C}$ <sup>28–31</sup>. We observed a clear motional narrowing effect associated with the intradomain carrier motion down to 4 K in the  $H_{\perp}$  configuration. For the  $H_{\parallel}$  configuration, the linewidth analyses based on the density functional theory (DFT) calculation of the *g* values show a clear signature of signal averaging associated with the interdomain carrier motion occurring down to at least 70 K. This efficient interdomain electrical connection should be realized by the rigid, nearly torsion-free backbone conformation, as demonstrated by the structural modeling with the DFT calculation.

## Results

**Device performance.** Figure 2 shows the results of transistor characteristics of the present DPP-based copolymers. Here, we adopt a top-gate device geometry with parylene gate insulators, as schematically illustrated in Fig. 2a, to avoid any operational instabilities, such as the gate-bias-stress effect<sup>52,53</sup>. We adopt an long rectangular substrate with dimensions of 3 mm × 30 mm, by which simultaneous measurements of the transistor characteristics and the FI-ESR measurements can be performed within the ESR sample tube<sup>42,47</sup>. In order to avoid the deterioration of the *Q*-factor of the ESR cavity, the thickness of the gate/source/drain electrodes was designed less than the skin depth of the microwave and the contacts and wirings were made at an end of the substrate, which is out of the sensitive part of the ESR cavity. The insulator film was formed on top of the polymer film using a chemical vapor deposition (CVD) method. This process does not affect the crystalline molecular order of the DPP-TVT film, as confirmed by the grazing-incidence X-ray diffraction (GIXD) pattern taken before and after the parylene deposition, as shown in Supplementary Fig. 1 and Supplementary Note 1. By using the above device structures, both polymer TFTs exhibit standard transfer and output characteristics as shown in Fig. 2b and c, respectively, for the DPP-TVT device and Fig. 2d, e, respectively, for the DPPT-TT device. The linear mobilities extracted from the transfer characteristics are  $\mu \sim 0.1 \text{ cm}^2 \text{ V}^{-1} \text{ s}^{-1}$  for both as-grown DPP-TVT and DPPT-TT devices, whereas higher mobilities of  $\sim 0.2 \text{ cm}^2 \text{ V}^{-1} \text{ s}^{-1}$  are reproducibly obtained in the DPP-TVT device annealed at 200 °C, which is consistent with the improved crystallinity<sup>32</sup>, as confirmed in the present study (Supplementary Fig. 1b).

**FI-ESR measurements.** Figure 3a, b shows the FI-ESR signals obtained for the PBTTT and DPP-TVT TFTs under the negative gate voltage ( $V_g$ ) of  $-100 \text{ V}$  at 150 K. The background signals

observed in the off state ( $V_g = +30 \text{ V}$ ) are subtracted from the signals in the on state. We observe clear FI-ESR signals of positive charge carriers (polarons) accumulated at the polymer/insulator interface. These signals exhibit clear anisotropies with respect to the applied magnetic field direction. In the case of PBTTT, a single ESR signal is observed in the  $H_{\perp}$  configuration, whereas a doubly split signal is observed in the  $H_{\parallel}$  configuration. This feature is typical of the edge-on-oriented molecules with an orthorhombic *g* anisotropy;<sup>50</sup> the doubly split signal in the  $H_{\parallel}$  configuration comes from the difference in the resonance magnetic field  $H_0$  ( $H_0 = h\nu/g\mu_B$ ;  $h$ : Planck's constant,  $\nu$ : microwave frequency, and  $\mu_B$ : Bohr magneton) due to the *g* anisotropy of  $g_z$  and  $g_y$ , whereas the single ESR signal in the  $H_{\perp}$  configuration comes from the  $g_x$  component, where *x*, *y*, and *z* directions correspond to the molecular short axis, long axis, and the  $\pi$ -orbital direction, respectively<sup>10–12,50</sup>. In addition, clear line splitting in the  $H_{\parallel}$  configuration indicates the minor contribution of the interdomain carrier hopping at 150 K. If the interdomain charge hopping is efficient, then the *g* anisotropy is averaged out, and a Lorentzian-shaped single ESR signal is expected in the  $H_{\parallel}$  configuration. Based on the conventional ESR theory<sup>54,55</sup>, signal averaging occurs under the condition of  $\tau_{\text{inter}}^{-1} > |g_y - g_z|\mu_B H/h$ , where  $\tau_{\text{inter}}$  represents the interdomain hopping time, which has been observed in PBTTT TFTs at high temperatures above  $\sim 200 \text{ K}$ <sup>50,56</sup>.

In contrast to the case of PBTTT, the FI-ESR spectrum obtained for the DPP-TVT device exhibits no line splitting in the  $H_{\parallel}$  configuration, as shown in Fig. 3b. The absence of line splitting in the  $H_{\parallel}$  configuration clearly demonstrates the efficient interdomain motion of charge carriers in the polycrystalline DPP-TVT film based on the following discussion.

**ESR line-shape analyses based on DFT calculations.** The FI-ESR signal of DPP-TVT exhibits a clear anisotropy of the *g* value,

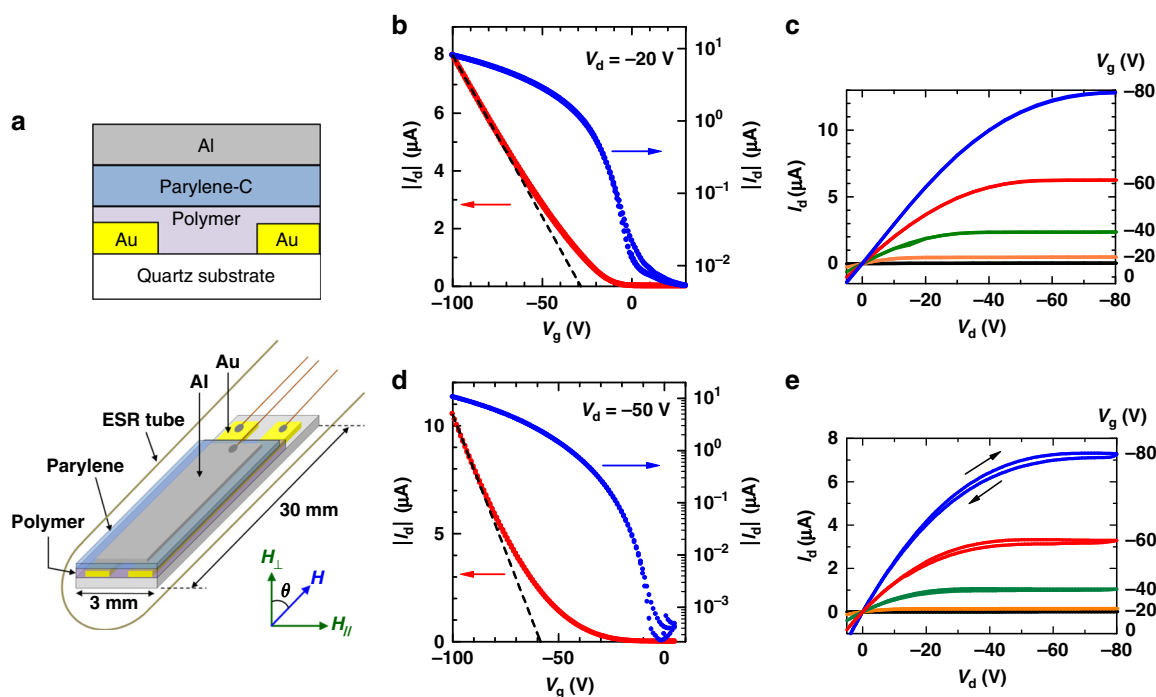


**Fig. 2** Transistor characteristics obtained at room temperature. **a** Schematic illustrations of the top-gate thin-film transistor (TFT) device.  $\theta$  denotes the angle between the magnetic field ( $\mathbf{H}$ ) and the substrate normal. **b**, **c** Typical transfer and output characteristics obtained for the annealed diketopyrrolopyrrole-thiophene-vinylene-thiophene (DPP-TVT) device at room temperature, respectively, and **d**, **e** those for diketopyrrolopyrrole-thiophene-thieno [3,2-*b*]thiophene (DPPT-TT) devices at room temperature. Here,  $I_d$ ,  $V_g$ , and  $V_d$  represent the drain current, gate voltage, and drain voltage, respectively. The source electrode is grounded

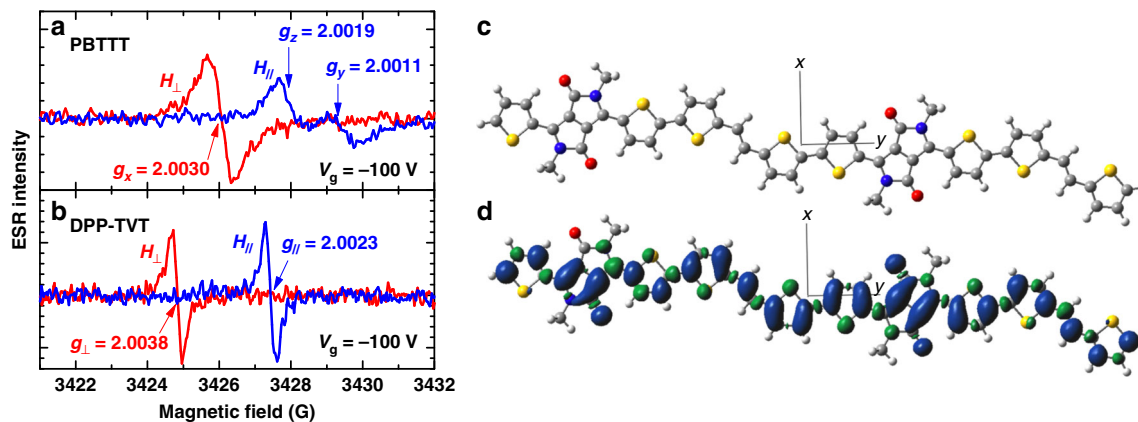


**Fig. 3** Typical field-induced electron spin resonance (FI-ESR) signals of representative polymer transistors and density functional theory (DFT) calculations for diketopyrrolo-pyrrole-thiophene-vinylene-thiophene (DPP-TVT). **a, b** Anisotropic FI-ESR signals obtained with the magnetic field parallel ( $H_{||}$ ) and perpendicular ( $H_{\perp}$ ) to the substrate at 150 K for the poly(2,5-bis(3-alkylthiophene-2-yl)thieno[3,2-b]thiophene) (PBT TT) and DPP-TVT devices, respectively. **c** DFT calculation of the optimized molecular structure of DPP-TVT and **d** spin density distribution (wave function) of the cation radical

indicating a certain molecular orientation at the insulator interface. The  $g$  values obtained with the  $H_{||}$  and  $H_{\perp}$  configurations correspond to the minimum and maximum values, as confirmed from the angular dependence measurements (Supplementary Note 2, Supplementary Fig. 2). The obtained extremal  $g$  values of DPP-TVT are  $g_{\perp} = 2.0038$  and  $g_{||} = 2.0023$ . Unfortunately, no direct information exists on the principal  $g$  values, which are essential to determine the molecular orientation<sup>42,46,51,57–60</sup>, for DPP-based copolymers. Thus, we adopted a computational method to obtain the principal  $g$  values based on DFT calculations.

DFT calculations of the  $g$  tensor were performed for oligomer models of DPPT-TVT and DPPT-TT. Figure 3c, d shows the optimized structure and spin density distribution, respectively, calculated by DFT method for a DPP-TVT oligomer with repeating unit number  $n = 2$ , and Table 1 summarizes the calculated principal  $g$  values for DPP-TVT, together with those of DPPT-TT. As in the case of PBT TT, the principal axes ( $x, y, z$ ) of the  $g$  tensor are along the molecular short axis, long axis, and the  $\pi$  orbital direction, respectively, as shown in Fig. 3c. The maximum  $g$  value is obtained along the  $x$ -axis, showing a fairly good agreement with the  $g_{\perp}$  value observed for DPP-TVT. This result indicates the edge-on orientation of the polymer backbone at the insulator interface, which is consistent with the previous X-ray structural analyses for the bulk film<sup>32</sup> and the GIXD patterns shown in Supplementary Fig. 1.

In the case of a uniaxial edge-on molecular orientation, we expect the ESR line splitting in the  $H_{||}$  configuration when the interdomain carrier motion is negligible, as in the case of PBT TT. We confirm that no line splitting signature is observed in the  $H_{||}$  and  $H_{\perp}$  configurations down to 4 K, as shown in Fig. 4a. In general, there are two possible explanations for the absence of the line splitting in the in-plane signal: (i) an intrinsically small  $g$  anisotropy of  $|g_y - g_z|$  gives only a small line splitting, which is masked by the natural linewidth in the target material, and (ii) the interdomain charge hopping averages out the split signals into a single line. For the former possibility, the DFT calculation of the  $g$  values provides crucial information; the  $g$  anisotropy of  $|g_y - g_z|$  shown in Table 1 indicates the in-plane line splitting of 0.67 G for  $n = 2$  and 1.1 G for  $n = 3$  of DPP-TVT at the X-band microwave frequency (9.6 GHz), which are sufficiently larger than the peak-to-peak linewidth ( $\Delta H_{pp}$ ) observed for these polymers at 150 K ( $\Delta H_{pp} = 0.3$  G for DPP-TVT). In this case, if the interdomain charge hopping is negligible, then a clear line splitting should be

**Table 1** Summary of the principal  $g$  values obtained by density functional theory calculation

	$g_x$	$g_y$	$g_z$
DPP-TVT ( $n = 2$ )	2.00417	2.00175	2.00214
DPP-TVT ( $n = 3$ )	2.00419	2.00151	2.00213
DPPT-TT ( $n = 3$ )	2.00433	2.00157	2.00212

DPP-TVT diketopyrrolo-pyrrole-thiophene-vinylene-thiophene, DPPT-TT diketopyrrolo-pyrrole-thiophene-thieno[3,2-b]thiophene

observed in the in-plane ESR signal. Therefore, the absence of this line splitting is clear evidence of efficient interdomain charge hopping at 150 K, in contrast to the case of PBT TT.

**Analyses of microscopic transport processes.** In this section, we provide a more detailed insight into the microscopic charge transport mechanism in DPP-TVT, for both intradomain and interdomain transport, based on the temperature dependence of the FI-ESR signal. Figure 4b, c shows the temperature dependence of the spin concentration  $N_{spin}$  and  $\Delta H_{pp}$ , respectively, obtained from the FI-ESR signals of the DPP-TVT device shown in Fig. 4a. The Arrhenius plot of the normalized  $\Delta H_{pp}$  is also shown in Fig. 4d. Here,  $N_{spin}$  is calculated from the spin susceptibility  $\chi$  by considering the Curie law ( $\chi = N_{spin} g^2 \mu_B^2 S(S+1)/3k_B T$ ;  $k_B$ : Boltzmann constant, and  $S = 1/2$ ), and it agrees well with the charge concentration ( $N_{charge}$ ) calculated from the insulator capacitance down to 4 K, as shown by the dashed line in Fig. 4b. This result indicates that the charge carriers are isolated polarons that have both spin and charge<sup>61</sup>. In this case, the hyperfine (hf) magnetic field originating from the proton and nitrogen nuclei on the polymer backbone causes a finite ESR line broadening. If the charge carriers are static, then the random distribution of the hf field produces a Gaussian-shaped ESR spectrum, whereas if the carriers are mobile, then the hf field is averaged out, and a Lorentzian-shaped narrow signal is produced<sup>54,55</sup>. This effect is known as motional narrowing, which can be used to probe the microscopic motion of charge carriers. In the case of edge-on oriented molecules, the ESR linewidth in the  $H_{\perp}$  configuration is not affected by the  $g$  anisotropy and only the hf field contributes to the linewidth; thus, the motional narrowing in this configuration reflects the information of the intradomain carrier motion within the ordered domains, even for the case in which



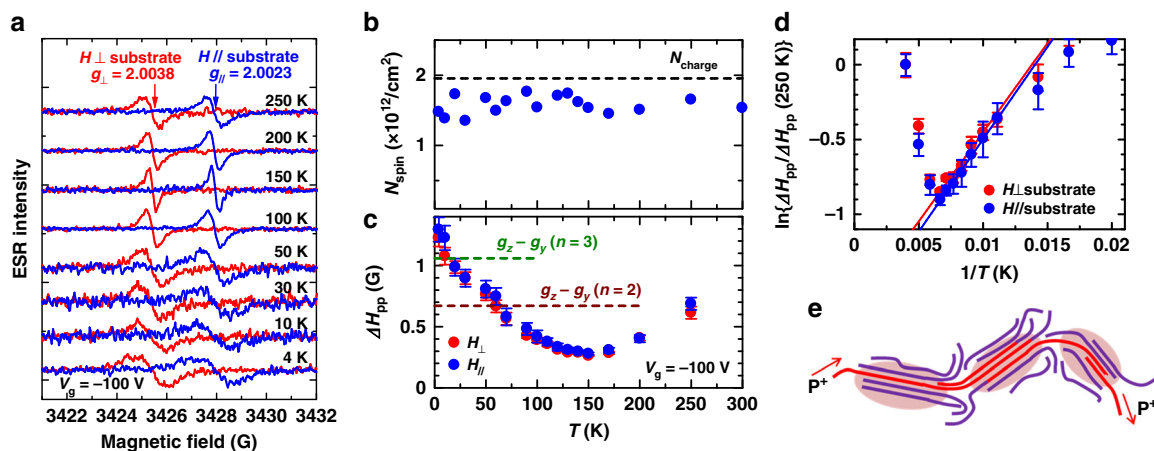


**Fig. 4** Field-induced electron spin resonance (FI-ESR) parameters for the diketopyrrolo-pyrrole-thiophene-vinylene-thiophene (DPP-TVTV) device. Temperature dependence of the **a** normalized FI-ESR signal obtained with the magnetic field parallel and perpendicular to the substrate, **b** accumulated spin concentration ( $N_{\text{spin}}$ ), and **c** FI-ESR linewidth ( $\Delta H_{\text{pp}}$ ) obtained for each magnetic field direction in the DPP-TVTV device. **d** Arrhenius plot of the normalized linewidth above 50 K. **e** Schematic illustration of the microscopic charge transport of polarons ( $P^+$ ) within the domains and across domain boundaries via tie molecules (shown in red) in donor-acceptor (DA) copolymers. The carriers can be fully delocalized within the domains due to strong  $\pi$ - $\pi$  interactions both in conventional semicrystalline polymers and DA polymers. However, the interdomain transport pathways are effectively formed in the case of DA polymers, which have a rigid, highly planar backbone. The dashed line in **b** shows the charge concentration ( $N_{\text{charge}}$ ) determined from the capacitance measurement. The dashed lines in **c** shows the difference in the resonance magnetic field arising from the anisotropy of the  $g$  values between the chain ( $g_y$ ) and  $\pi$ -stack ( $g_z$ ) directions calculated by the DFT method for the DPP-TVTV with  $n = 2$  and 3. The solid lines in **d** show the linear fitting of the data to the activation formulae between 70 and 150 K in both directions. Error bars represent the uncertainty in determining the linewidth due to the noise level of the FI-ESR signal

the domain boundaries limit the macroscopic transport by the poor interdomain connectivity<sup>50</sup>.

As shown in Fig. 4c,  $\Delta H_{\text{pp}}$  in the  $H_{\perp}$  configuration exhibits a clear narrowing below 150 K as the temperature is increased, indicating intradomain motional narrowing. Above 150 K, a line broadening is observed contrary to the motional narrowing, resulting in the minimum of the linewidth at 150 K. This line broadening is due to the shortening of the spin-lattice relaxation time through the spin-phonon interaction, which is beyond the scope of the present analyses<sup>46,49,51</sup>. In the extreme narrowing condition of  $\gamma (\Delta H_{\text{d}})\tau_{\text{c}} \ll 1$ , the motional narrowed ESR linewidth is described in Eq. (1):

$$\frac{\sqrt{3}}{2} \Delta H_{\text{pp}} = \gamma (\Delta H_{\text{d}})^2 \tau_{\text{c}},$$

where  $\Delta H_{\text{d}}$  is the half-width at half-maximum of the static linewidth without narrowing,  $\tau_{\text{c}}$  is the spin correlation time, and  $\gamma$  is the gyromagnetic ratio of the electron<sup>55</sup>. Considering the trap-and-release processes of charge carriers,  $\tau_{\text{c}}$  can be identified with the trapping time ( $\tau_{\text{tr}}$ ) of the carrier,<sup>48,57</sup> which becomes shorter for higher temperatures.

The observed  $\Delta H_{\text{pp}}$  in the  $H_{\perp}$  configuration displays an activation behavior in the temperature range of 100 K  $< T <$  150 K, as shown in Fig. 4d, with an activation energy ( $E_{\text{a}}^{\text{intra}}$ ) of 10.6 meV. This value is smaller than those observed in the semicrystalline polymer PBTTT ( $E_{\text{a}}^{\text{intra}} = 21$  meV for the TFT with an  $\text{SiO}_2$  insulator<sup>50</sup> and  $E_{\text{a}}^{\text{intra}} = 17$  meV for the device using a parylene insulator<sup>56</sup>). Although the microscopic motion of the carriers depends strongly on the insulator material, as demonstrated in Supplementary Fig. 3 and Supplementary Note 3 using the  $\text{Al}_2\text{O}_3$  insulator, the smaller  $E_{\text{a}}^{\text{intra}}$  value in the present DPP-TVTV device than that in the semicrystalline PBTTT device using the parylene insulator indicates the highly mobile nature of charge carriers within the ordered domains with small trap energies in DPP-TVTV. This result is also supported by the fact that we observe a signature of motional narrowing even at approximately 4 K, as shown in Fig. 4c, although the detailed

origin of the trap energy, which should be related to the defects or disorders within the crystalline domains, is still unclear at present. In fact, we observe an FI-ESR signal that is close to the Lorentzian signal at 4 K, as shown in Supplementary Fig. 3, for the device using a parylene insulator, which is characteristic of the motionally narrowed ESR signal.

In contrast to the FI-ESR signal in the  $H_{\perp}$  configuration, the linewidth in the  $H_{\parallel}$  configuration contains the contribution from the  $g$  anisotropy of  $|g_y - g_z|$  in addition to the hf interaction, as already mentioned, which is not averaged out by the intradomain carrier motion but by the interdomain carrier motion among the randomly aligned domains<sup>50,51</sup>. As in the case of the  $H_{\perp}$  configuration, the motionally narrowed in-plane ESR linewidth is described by Eq. (1). When the hyperfine interaction is sufficiently averaged by the intradomain charge motion,  $\Delta H_{\text{d}}$  in Eq. (1) is dominated by the difference in the resonance magnetic field due to the  $g$  anisotropy of  $g_y$  and  $g_z$  (hereafter defined as  $\Delta g$  width) and  $\tau_{\text{c}}$  in this case is identified as  $\tau_{\text{inter}}$ <sup>55</sup>. In the low-temperature region, the observed linewidth is larger than the  $\Delta g$  width expected from the  $g$  anisotropy in Table 1, as shown by the dashed lines in Fig. 4c. In this case,  $\Delta H_{\text{d}}$  in Eq. (1) is dominated by the hf interaction and the motional narrowing reflects the intradomain carrier motion even in the  $H_{\parallel}$  configuration. On the other hand, the observed in-plane linewidth shown in Fig. 4c becomes narrower than the  $\Delta g$  widths above  $\sim 70$  K. In this temperature region, the  $\Delta g$  width is even larger than the hf-determined linewidth observed in the  $H_{\perp}$  configuration due to the prominent averaging effect of the hf interaction by the intradomain carrier motion. In this case, if the interdomain carrier motion is negligible, clear line splitting by the  $\Delta g$  width should be expected as already mentioned, whereas no such splitting is observed in Fig. 4a. This clearly indicates the occurrence of the interdomain carrier hopping, which averages out the  $\Delta g$  width, at least above  $\sim 70$  K.

Next, we compare the intradomain and interdomain charge transport processes based on the activation energies of these

**Table 2 Summary of activation energies of microscopic and macroscopic charge transport processes**

	$E_a^{\text{intra}}$ (meV)	$E_a^{\text{inter}}$ (meV)	$E_a^{\mu}$ (meV)
DPP-TVT	10.6	10.3	74
DPPT-TT	13.6	11.9	68
PBTTT/SiO <sub>2</sub> (ref. 50)	21	86	90

DPP-TVT diketopyrrolo-pyrrole-thiophene-vinylene-thiophene, DPPT-TT diketopyrrolo-pyrrole-thiophene-thieno[3,2-b]thiophene, PBTTT poly(2,5-bis(3-alkylthiophene-2-yl)thieno[3,2-b]thiophene)

processes. Interestingly, the temperature dependences of  $\Delta H_{\text{pp}}$  for the  $H_{\perp}$  and  $H_{\parallel}$  configurations are almost identical, as shown in Fig. 4c, d, for DPP-TVT. The extracted activation energy  $E_a^{\text{inter}}$  of the interdomain charge transport is 10.3 meV, which is almost the same value as that of  $E_a^{\text{intra}}$  obtained for the same device, as summarized in Table 2 together with those of DPPT-TT and those reported for the PBTTT TFTs<sup>50</sup>. This agreement is surprising considering the fact that the boundary of the differently aligned domains is usually the major limiting factor of the macroscopic charge transport, which is clearly demonstrated for the PBTTT devices by the FI-ESR results<sup>50</sup>. In the case of PBTTT,  $E_a^{\text{inter}}$  is much larger than  $E_a^{\text{intra}}$ , and it is close to the mobility activation energy ( $E_a^{\mu}$ ), as shown in Table 2, giving clear evidence of boundary-limited charge transport. In contrast to the case of the PBTTT device, the present results indicate that the interdomain charge transport is as efficient as intradomain charge transport. In other words, no excess energy is necessary for the charge transport across the domain boundaries from a microscopic viewpoint. Thus, this result clearly demonstrates the superior connectivity of the domains through the tie molecules in DPP-TVT, which is schematically illustrated in Fig. 4e.

**Structural modeling by DFT calculations.** Here, we discuss the structural origin of the efficient intradomain and interdomain charge transport processes realized in the present DPP-TVT device based on the DFT calculation. Figure 5 summarizes the structural optimization of a single DPP-TVT unit. The DPP-TVT backbone exhibits a highly planar conformation with fairly small torsion angles (shown in Fig. 5a) between the subunits, the torsion potential of which are given in Fig. 5b. In the lowest-energy conformation, the torsion of each subunit is almost negligible. Although the DPP-based copolymers still show some energetic disorders presumably arising from the finite backbone torsion in the actual film<sup>38,62</sup>, this structural feature is in contrast to the case of PBTTT, where a finite torsion angle between the thienothiophene and thiophene units is expected from the similar structural optimization<sup>38</sup>. The nearly torsion-free molecular conformation of DPP-TVT results in a rather delocalized nature of the carrier wave function within the chain, as reflected in the spin density distribution of the cationic state shown in Fig. 3d. The delocalized nature of the carrier wave function is advantageous for the on-chain carrier motion, which might be reflected in the small activation energy of the microscopic charge motions in DPP-TVT.

In addition, face-to-face packing of the coplanar backbone can promote interchain charge transfer, which is essential for large-scale charge transport because of the finite chain length of the actual polymers. Although the interchain hopping of the carriers cannot be observed directly from the present FI-ESR measurements, the efficient interchain charge delocalization is demonstrated by our DFT calculation of the spin density distribution considering face-to-face-packed, two oligomer chains, as shown

in Supplementary Fig. 4 and Supplementary Note 4. In this calculation, we clearly observe a delocalization of the carrier wave function of the positive polaron ( $P^+$ ) to the adjacent polymer chain. It is also noteworthy that the principal  $g$  values calculated based on this delocalized state between two chains are  $g_x = 2.0037$ ,  $g_y = 2.0017$ , and  $g_z = 2.0021$ , where the  $g_x$  value is closer to the experimental  $g_{\perp}$  value than that calculated by considering only a single chain ( $g_x = 2.0042$ ), whereas the other two components are unchanged. This result supports the concept that the carriers are delocalized to the adjacent chains within the ordered domains in the actual DPP-TVT film.

In addition to the above discussion, the highest impact of the torsion-free backbone on the charge transport lies in the electrical connection of the adjacent domains as a tie molecule. In general, torsion of the backbone prevents the  $\pi$ - $\pi$  interaction, especially in the amorphous regions, which limits the interdomain electrical connectivity<sup>39</sup>. However, the domain boundaries are not the limiting factor of the interdomain charge transport in DPP-TVT TFTs. Since the high backbone planarity is also expected in the amorphous region because the present structural optimization is performed for the single isolated chain, it is natural to consider that this high planarity of the present polymer is also responsible for the high electrical domain connectivity, in addition to the strong interchain interaction generally expected between the donor and acceptor units in the DA copolymers<sup>23,24,36</sup>. In contrast, the backbone planarity of the PBTTT in the amorphous region is low, which limits the mobility as demonstrated by the molecular dynamics simulation<sup>63</sup>, resulting an inferior domain connectivity in the case of PBTTT.

The charge transport processes mentioned above are also summarized in Fig. 4e, i.e., the charges can be delocalized within the domains through the strong intermolecular  $\pi$ - $\pi$  interactions and can be transported to adjacent domains by the high on-chain mobility of the highly planar tie molecules. The planar backbone can also promote the face-to-face packing of the backbones, even in the amorphous region, thus improving the domain connectivity. In contrast, the finite backbone torsion of PBTTT prevents the efficient connection of the domains, thus limiting the macroscopic charge transport. However, the intradomain charge transport is not severely affected by the backbone torsion, which was demonstrated by our previous FI-ESR measurement revealing that the intradomain carrier motion is not frozen, even at 4 K, in the PBTTT TFTs on the parylene insulator<sup>56</sup>. Therefore, the backbone torsion more severely affects the interdomain transport than the intradomain charge transport by limiting the on-chain carrier motion of the tie molecules.

The above discussion is also applicable to DPPT-TT. Figure 6 shows the FI-ESR results of DPPT-TT devices with the parylene insulator. We observed an anisotropic ESR signal with the extremal  $g$  values of  $g_{\perp} = 2.0040$  and  $g_{\parallel} = 2.0024$ . Based on the DFT calculation shown in Table 1, the observed  $g_{\perp}$  agrees well with the  $g_x$  value, strongly indicating that the carriers accumulate in the region with the edge-on molecular orientation, as in the DPP-TVT device, even though the bulk film tends to show structural disorders in this polymer<sup>28-30</sup>. In addition, no line splitting is observed down to 4 K both in the  $H_{\perp}$  and  $H_{\parallel}$  configurations, as shown in Fig. 6a. Since the ESR linewidth in the  $H_{\parallel}$  configuration in Fig. 6b becomes narrower than the line splitting expected from the  $g$  anisotropy in Table 1 (0.94 G at the X-band, as shown by the dashed line in Fig. 6b), an efficient interdomain charge transport is again demonstrated down to  $\sim 70$  K in the DPPT-TT devices. Furthermore, the activation energies of the intradomain and interdomain carrier motion, which are obtained from the Arrhenius plot of the normalized linewidth in the  $H_{\perp}$  and  $H_{\parallel}$  configurations in Fig. 6c, respectively, agree well with each other, as shown in Table 2. Therefore, efficient

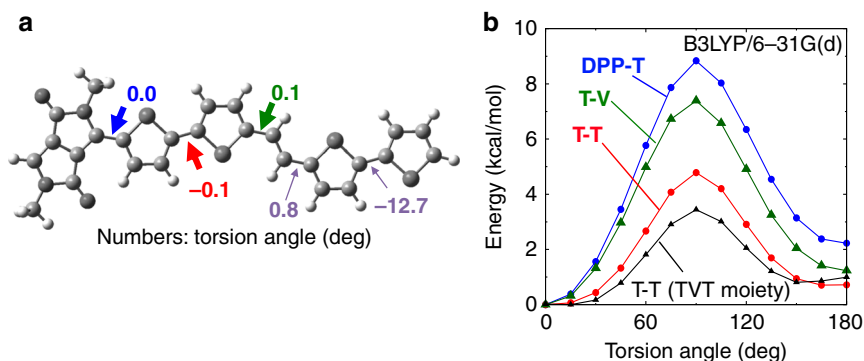


**Fig. 5** Structural optimization of the diketopyrrolo-pyrrole-thiophene-vinylene-thiophene (DPP-TVT) monomer. **a** Density functional theory (DFT)-calculated optimized molecular structure of the DPP-TVT monomer together with optimized torsion angles. **b** DFT-calculated torsion potentials between DPP and adjacent thiophene units (DPP-T), thiophene-vinylene units (T-V), thiophene-thiophene units, together with the torsion potentials between thiophene-thiophene (T-T) units calculated for the isolated TVT moiety

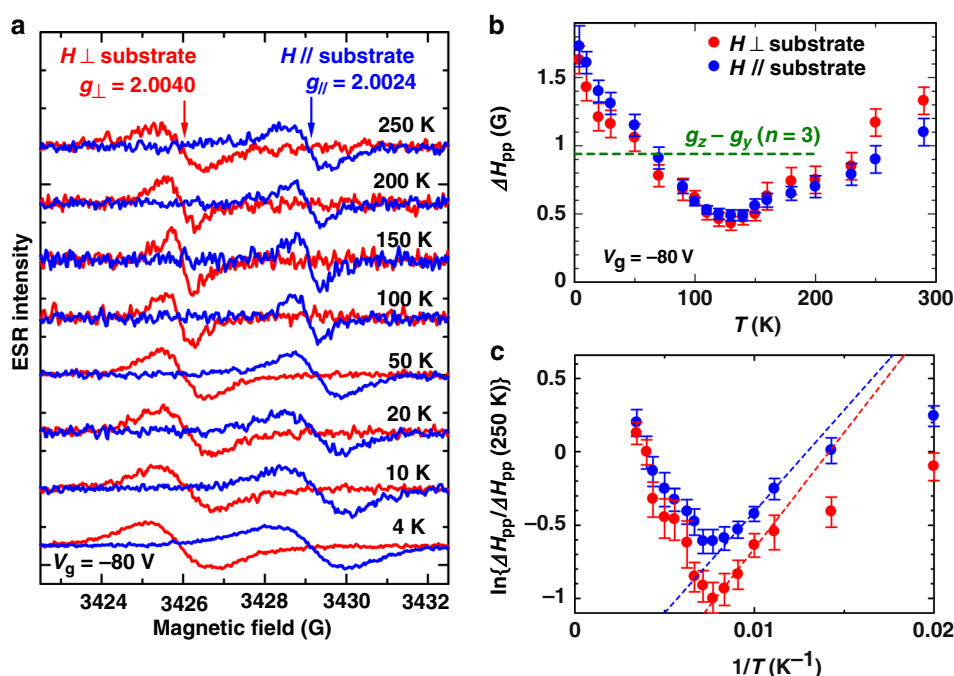


**Fig. 6** Field-induced electron spin resonance (FI-ESR) parameters for the diketopyrrolo-pyrrole-thiophene-thieno[3,2-*b*]thiophene (DPPT-TT) device. Temperature dependence of the **a** normalized FI-ESR signal obtained with the magnetic field parallel and perpendicular to the substrate and **b** FI-ESR linewidth ( $\Delta H_{pp}$ ) obtained for each magnetic field direction. **c** Arrhenius plot of the normalized linewidth above 50 K in the DPPT-TT device. Error bars represent the uncertainty in determining the linewidth due to the noise level of the FI-ESR signal

intradomain carrier motion is extended to adjacent domains with different chain alignments through rigid tie molecules in DPPT-TT devices. The planar backbone conformation of DPPT-TT has also been reported<sup>64</sup>, which is consistent with the above observations.

## Discussion

Here, we compare the microscopic carrier dynamics clarified by the FI-ESR measurements to the macroscopic charge transport observed in the same devices. We measured the activation energy of the mobility from the temperature dependence of the transfer characteristics shown in Supplementary Fig. 5 and Supplementary Note 5 for both polymer TFTs. The results are also shown in Table 2. Here, the observed activation energies are  $E_a^\mu = 74$  and 68 meV for the DPP-TVT and DPPT-TT devices, respectively.

Although these values are similar to those usually observed for the semicrystalline polymers and the high-mobility DA copolymers<sup>14</sup>, they are much larger than those of the intradomain and interdomain charge transport processes obtained by the present FI-ESR measurements. In other words, the microscopic charge transport process is still different from the macroscopic process in the present DPP-based devices, even though the interdomain transport is highly efficient. This result indicates the presence of another limiting factor of macroscopic charge transport. Although the detailed origin of this limiting factor is unclear, relatively large-scale domain or grain structures of the film should be responsible. For example, the surface of the DPP-TVT film exhibits a granular structure with the typical grain size on the order of  $\sim 100$  nm, as shown in Supplementary Fig. 6 and Supplementary Note 6. This rough film surface can be a limiting factor of macroscopic charge transport, especially in the case of

top-gate devices, as in the present study. This phenomenon is also consistent with the fact that the FI-ESR signal of DPP-TVT exhibits almost no change before and after annealing at 200 °C, as shown in Supplementary Fig. 7 and Supplementary Note 7, even though both the crystallinity and the room temperature mobility are improved by annealing. This result indicates that the microscopic properties or dynamics of charge carriers, as well as the local molecular orientation around them, are almost unchanged, whereas large-scale structural changes, which are reflected in the GIXD profiles in Supplementary Fig. 1, affect the mobility. However, we emphasize that the microscopic transport properties obtained by the present FI-ESR measurements indicate that the charge transport ability in the present DPP-based copolymers is potentially quite high, meaning that they can be suitably applied to high-mobility organic electronic devices if adequate optimizations of the film morphology are carried out.

In summary, we performed FI-ESR measurements on the TFT devices of DA-type DPP-based conjugated polymers, DPP-TVT and DPPT-TT, to clarify the microscopic charge transport properties. Even though the macroscopic charge transport should be limited by the large-scale grain structure of the films, information of the highly mobile charge carriers realized within the crystalline domains was extracted by the FI-ESR measurements. The carrier motion within the domains was observed down to 4 K, where the macroscopic TFT operation was not observed. The activation energy of the intradomain carrier motion was as low as ~10 meV, which is lower than those in conventional semicrystalline polymers. Such small trapping energy is reasonably ascribed to the highly planar molecular structures theoretically expected from DFT calculations. Furthermore, the high molecular planarity also results the efficient electrical connection between the crystalline domains. The activation energy of the interdomain carrier motion, obtained by the motional narrowing effect of the in-plane ESR linewidth, was almost the same as that of the intradomain motion. The same activation energy between the intradomain and interdomain carrier motion indicates that these processes are essentially identical with each other, i.e., the on-chain carrier motion within and across the domains is observed as the dominant contributions to the motional narrowing effect. The present FI-ESR method is therefore a powerful tool to probe the intrinsic transport properties which cannot be accessed by the macroscopic transport measurements.

## Methods

**Sample preparation.** Samples of PBTTT with hexadecyl side chains ( $M_w = 73,700\text{--}82,800$ ) were purchased from Merck Co. Ltd. Samples of DPP-TVT ( $M_w = 50,000$ , PDI = 2.4) were purchased from 1-Materials Co. Ltd. DPPT-TT ( $M_n = 70,000$ , PDI = 3.13) was synthesized in house, and details of this procedure are described in a previous paper<sup>65</sup>. The TFTs with the top-gate device geometry shown in Fig. 2a were fabricated on a 3 mm × 30 mm quartz substrate as follows. The substrate was first cleaned by sonicating in deionized water, acetone, and 2-propanol for 5 min each. In the case of PBTTT, the polymer layer was fabricated by drop casting the 4 mg/ml *o*-dichlorobenzene solution followed by annealing (180 °C, 15 min) on the substrate patterned by 30-nm-thick Au source/drain electrodes. In the case of DPP-TVT, the drop cast film was fabricated using a 3 mg/ml chlorobenzene solution. We prepared both the as-grown film without annealing and the annealed film (200 °C, 2 h) to modify the crystallinity. For the DPPT-TT film, a 10 mg/ml dichlorobenzene solution was spin coated on the substrate at 1500 r.p.m., followed by annealing (120 °C, 1 h) to remove the solvent. Then, a thin-film of parylene-C with a thickness less than 1 μm was fabricated on these polymer films as a gate insulator by CVD. The insulator capacitance was 2.8 nF cm<sup>-2</sup> for the PBTTT device, 3.8 nF cm<sup>-2</sup> for the DPP-TVT device, and 4.4 nF cm<sup>-2</sup> for the DPPT-TT device. Finally, an Al gate (G) electrode was vapor deposited. In the case of DPP-TVT, a bottom gate, top-contact device was also prepared using a 300-nm-thick Al<sub>2</sub>O<sub>3</sub> insulator with an Al gate electrode. The channel length (*L*) and width (*W*) were *L* = 1.4 mm and *W* = 19 mm for the PBTTT and DPPT-TT devices and *L* = 1.4 mm and *W* = 15 mm for the DPP-TVT device. The fabricated device was inserted into the ESR sample tube and sealed with 100 Torr He gas for thermal exchange.

**Device characterization.** The GIXD measurements were performed using a Rigaku FR-E Micro-focus High Intensity X-ray Generator system with a CuKα X-

ray source ( $\lambda = 1.5418 \text{ \AA}$ ) at the High Intensity X-ray Diffraction Laboratory (HIX) at Nagoya University. The in-plane and out-of-plane diffractions were detected by an imaging plate. TFT characteristics were measured using a Keithley 2612A source measuring unit. ESR measurements were performed using a Bruker E-500 X-band spectrometer equipped with an Oxford ESR 900 gas-flow-type cryostat. The gate voltage was applied by using a Keithley 2612A source measuring unit. For the angular-dependence measurements, the ESR sample tube with the TFT device was rotated with respect to the applied magnetic field direction inside the ESR cavity equipped with a home-made protractor, which is schematically illustrated in Fig. 2a. For the low-temperature FI-ESR measurements, the gate voltage was applied at room temperature with the source and drain electrodes being short circuited, and then the system was cooled down during the application of the gate voltage.

**DFT calculation.** DFT calculations of the *g* tensor for a DPP-TVT oligomer with repeat unit number  $n = 2$  (see Fig. 3c) were performed with the UB3LYP functional and 6-31 G(d) basis set. To reduce finite chain-length effects, we also carried out calculations for longer oligomers with  $n = 3$  at the UB3LYP/6-311++G(d,p)//UB3LYP/6-31G(d) level for DPP-TVT as well as DPPT-TT. The alkyl side chains on the DPP units were replaced with methyl groups. The calculations were carried out using the Gaussian 09 and Gaussian 16 software packages<sup>66</sup>.

## Data availability

The data that support the findings of this study are available from the corresponding authors upon reasonable request

Received: 25 March 2019 Accepted: 29 July 2019

Published online: 19 August 2019

## References

- Wolf, U., Bassler, H., Borsenberger, P. M. & Gruenbaum, W. T. Hole trapping in molecularly doped polymers. *Chem. Phys.* **222**, 259–267 (1997).
- Novikov, S. V., Dunlap, D. H., Kenkre, V. M., Parris, P. E. & Vannikov, A. V. Essential role of correlations in governing charge transport in disordered organic materials. *Phys. Rev. Lett.* **81**, 4472–4475 (1998).
- Salleo, A., Chabiny, M. L., Yang, M. S. & Street, R. A. Polymer thin-film transistors with chemically modified dielectric interfaces. *Appl. Phys. Lett.* **81**, 4383–4385 (2002).
- Veres, J., Ogier, S., Lloyd, G. & Leeuw, D. Gate insulators in organic field-effect transistors. *Chem. Mater.* **16**, 4543–4555 (2004).
- Sirringhaus, H. Device physics of solution-processed organic field-effect transistors. *Adv. Mater.* **17**, 2411–2425 (2005).
- Street, R. A., Northrup, J. E. & Salleo, A. Transport in polycrystalline polymer thin-film transistors. *Phys. Rev. B* **71**, 165202 (2005).
- Bao, Z. & Locklin, J. *Organic Field-Effect Transistors*. (CRC Press, Boca Raton, 2007).
- Bao, Z., Dodabalapur, A. & Lovinger, A. J. Soluble and processable regioregular poly(3-hexylthiophene) for thin film field-effect transistor applications with high mobility. *Appl. Phys. Lett.* **69**, 4108–4110 (1996).
- Sirringhaus, H. et al. Two-dimensional charge transport in self-organized, high-mobility conjugated polymers. *Nature* **401**, 685–688 (1999).
- McCulloch, I. et al. Liquid-crystalline semiconducting polymers with high charge-carrier mobility. *Nat. Mater.* **5**, 328–333 (2006).
- Salleo, A., Kline, R. J., DeLongchamp, D. M. & Chabiny, M. L. Microstructural characterization and charge transport in thin films of conjugated polymers. *Adv. Mater.* **22**, 3812–3838 (2010).
- Umeda, T., Kumaki, D. & Tokito, S. Surface-energy-dependent field-effect mobilities up to 1 cm<sup>2</sup>/Vs for polymer thin-film transistor. *J. Appl. Phys.* **105**, 024516 (2009).
- Rivnay, J. et al. A structural origin of gap states in semicrystalline polymers and the implications for charge transport. *Phys. Rev. B* **83**, 121306 (2011).
- Noriega, R. et al. A general relationship between disorder, aggregation and charge transport in conjugated polymers. *Nat. Mater.* **12**, 1038–1044 (2013).
- Puntambekar, K. P., Pesanento, P. V. & Frisbie, C. D. Surface potential profiling and contact resistance measurements on operating pentacene thin-film transistors by Kelvin probe force microscopy. *Appl. Phys. Lett.* **83**, 5539–5541 (2003).
- Kline, R. J. et al. Dependence of regioregular poly(3-hexylthiophene) film morphology and field-effect mobility on molecular weight. *Macromolecules* **38**, 3312–3319 (2005).
- Chang, J. F. et al. Molecular-weight dependence of interchain polaron delocalization and exciton bandwidth in high-mobility conjugated polymers. *Phys. Rev. B* **74**, 115318 (2006).



18. Hallam, T. et al. Local charge trapping in conjugated polymers resolved by scanning kelvin probe microscopy. *Phys. Rev. Lett.* **103**, 256803 (2009).
19. Pingel, P. et al. Temperature-resolved local and macroscopic charge carrier transport in thin P3HT layers. *Adv. Funct. Mater.* **20**, 2286–2295 (2010).
20. Mollinger, S. A., Krajina, B. A., Noriega, R., Salleo, A. & Spakowitz, A. J. Percolation, tie-molecules, and the microstructural determinants of charge transport in semicrystalline conjugated polymers. *ACS Macro Lett.* **4**, 708–712 (2015).
21. Wang, H. et al. Structure and morphology control in thin films of conjugated polymers for an improved charge transport. *Polymers* **5**, 1272–1324 (2013).
22. Sirringhaus, H. 25th Anniversary Article: Organic field-effect transistors: the path beyond amorphous silicon. *Adv. Mater.* **26**, 1319–1335 (2014).
23. Himmelberger, S. & Salleo, A. Engineering semiconducting polymers for efficient charge transport. *MRS Commun.* **5**, 383–395 (2015).
24. Tsao, H. N. et al. Plastic electronics: the influence of morphology on high-performance polymer field-effect transistors. *Adv. Mater.* **21**, 209–212 (2009).
25. Yamashita, Y. et al. Mobility exceeding  $10 \text{ cm}^2/(\text{V}\cdot\text{s})$  in donor-acceptor polymer transistors with band-like charge transport. *Chem. Mater.* **28**, 420–424 (2016).
26. Rivnay, J. et al. Unconventional face-on texture and exceptional in-plane order of a high mobility n-type polymer. *Adv. Mater.* **22**, 4359–4363 (2010).
27. Takacs, C. J. et al. Remarkable order of a high-performance polymer. *Nano Lett.* **13**, 2522–2527 (2013).
28. Li, Y., Singh, S. P. & Sonar, P. A high mobility p-type DPP-thieno[3,2-b]thiophene copolymer for organic thin-film transistors. *Adv. Mater.* **22**, 4862–4866 (2010).
29. Bronstein, H. et al. Thieno[3,2-b]thiophene-diketopyrrolopyrrole-containing polymers for high-performance organic field-effect transistors and organic photovoltaic devices. *J. Am. Chem. Soc.* **133**, 3272–3275 (2011).
30. Chen, Z. et al. High-performance ambipolar diketopyrrolopyrrole-thieno[3,2-b]thiophene copolymer field-effect transistors with balanced hole and electron mobilities. *Adv. Mater.* **24**, 647–652 (2012).
31. Li, J. et al. A stable solution-processed polymer semiconductor with record high-mobility for printed transistors. *Sci. Rep.* **2**, 754 (2012).
32. Chen, H. et al. Highly  $\pi$ -extended copolymers with diketopyrrolopyrrole moieties for high-performance field-effect transistors. *Adv. Mater.* **24**, 4618–4622 (2012).
33. Khim, D. et al. Simple bar-coating process for large-area, high-performance organic field-effect transistors and ambipolar complementary integrated circuits. *Adv. Mater.* **25**, 4302–4308 (2013).
34. Yoo, D. et al. Timely synthetic tailoring of biaxially extended thiylenevinylene-like polymers for systematic investigation on field-effect transistors. *Adv. Funct. Mater.* **25**, 586–596 (2015).
35. Yun, H.-J. et al. Dramatic inversion of charge polarity in diketopyrrolopyrrole-based organic field-effect transistors via a simple nitrile group substitution. *Adv. Mater.* **23**, 7300–7307 (2014).
36. Nielsen, C. B., Turbiez, M. & McCulloch, I. Recent advances in the development of semiconducting DPP-containing polymers for transistor applications. *Adv. Mater.* **25**, 1859–1880 (2013).
37. Zhang, X. et al. Molecular origin of high field-effect mobility in an indacenodithiophene-benzothiadiazole copolymer. *Nat. Commun.* **4**, 2238 (2013).
38. Venkateshvaran, D. et al. Approaching disorder-free transport in high-mobility conjugated polymers. *Nature* **515**, 384–388 (2014).
39. Son, S. Y. et al. High-field-effect mobility of low-crystallinity conjugated polymers with localized aggregates. *J. Am. Chem. Soc.* **138**, 8096–8103 (2016).
40. Zhang, X. et al. In-plane liquid crystalline texture of high-performance thienothiophene copolymer thin films. *Adv. Funct. Mater.* **20**, 4098–4106 (2010).
41. Carbone, P. & Troisi, A. Charge diffusion in semiconducting polymers: analytical relation between polymer rigidity and time scales for intrachain and interchain hopping. *J. Phys. Chem. Lett.* **5**, 2637–2641 (2014).
42. Marumoto, K. et al. Electron spin resonance of field-induced polarons in regioregular poly(3-alkylthiophene) using metal-insulator-semiconductor diode structures. *J. Phys. Soc. Jpn.* **74**, 3066–3076 (2005).
43. Marumoto, K., Kuroda, S., Takenobu, T. & Iwasa, Y. Spatial extent of wave functions of gate-induced hole carriers in pentacene field-effect devices as investigated by electron spin resonance. *Phys. Rev. Lett.* **97**, 256603 (2006).
44. Tanaka, H., Watanabe, S., Ito, H., Marumoto, K. & Kuroda, S. Direct observation of the charge carrier concentration in organic field-effect transistors by electron spin resonance. *Appl. Phys. Lett.* **94**, 103308 (2009).
45. Watanabe, S. et al. Electron spin resonance observation of field-induced charge carriers in ultrathin film transistors of regioregular poly(3-hexylthiophene) with controlled in-plane chain orientation. *Appl. Phys. Lett.* **96**, 173302 (2010).
46. Tanaka, H. et al. Observation of field-induced charge carriers in high-mobility organic transistors of a thienothiophene-based small molecule: electron spin resonance measurements. *Phys. Rev. B* **84**, 081306 (2011).
47. Tanaka, H. et al. Electron spin resonance observation of charge carrier concentration in organic field-effect transistors during device operation. *Phys. Rev. B* **87**, 045309 (2013).
48. Matsui, H., Hasegawa, T. & Tokura, Y. Polaron motional narrowing of electron spin resonance in organic field-effect transistors. *Phys. Rev. Lett.* **100**, 126601 (2008).
49. Tsurumi, J. et al. Coexistence of ultra-long spin relaxation time and coherent charge transport in organic single-crystal semiconductors. *Nat. Phys.* **13**, 994–998 (2017).
50. Matsui, H. et al. Correlation between interdomain carrier hopping and apparent mobility in polycrystalline organic transistors as investigated by electron spin resonance. *Phys. Rev. B* **85**, 035308 (2012).
51. Kinoshita, Y., Tanaka, H., Shimoi, Y., Takimiya, K. & Kuroda, S. Low-temperature carrier dynamics in high-mobility organic transistors of alkylated dinaphtho-thienothiophene as investigated by electron spin resonance. *Appl. Phys. Lett.* **105**, 033301 (2014).
52. Bobbert, P. A., Sharma, A., Mathijssen, S. G. J., Kemerink, M. & de Leeuw, D. M. Operational stability of organic field-effect transistors. *Adv. Mater.* **24**, 1146–1158 (2012).
53. Tanaka, H., Sawada, E., Azuma, K. & Kuroda, S. Direct probing of gate-bias stress effect in organic transistors by electron spin resonance spectroscopy. *Appl. Phys. Express* **8**, 051603 (2015).
54. Anderson, P. W. A mathematical model for the narrowing of spectral lines by exchange or motion. *J. Phys. Soc. Jpn.* **9**, 316–339 (1954).
55. Kubo, R. & Tomita, K. A general theory of magnetic resonance absorption. *J. Phys. Soc. Jpn.* **9**, 888–919 (1954).
56. Kawamura, S., Wakamatsu, A., Kuroda, S., Takenobu, T. & Tanaka, H. Microscopic observation of highly mobile charge carriers in organic transistors of semicrystalline conducting polymers. *Jpn. J. Appl. Phys.* **57**, 02CA04 (2017).
57. Marumoto, K. et al. Microscopic mechanisms behind the high mobility in rubrene single-crystal transistors as revealed by field-induced electron spin resonance. *Phys. Rev. B* **83**, 075302 (2011).
58. Tanaka, H., Hirate, M., Watanabe, S. & Kuroda, S. Microscopic signature of metallic state in semicrystalline conjugated polymers doped with fluoroalkylsilane molecules. *Adv. Mater.* **26**, 2376–2383 (2014).
59. Tanaka, H., Nishio, S., Ito, H. & Kuroda, S. Microscopic signature of insulator-to-metal transition in highly doped semicrystalline conducting polymers in ionic-liquid-gated transistors. *Appl. Phys. Lett.* **107**, 243302 (2015).
60. Shimoi, Y., Marumoto, K. & Kuroda, S. Theoretical ESR g values in rubrene and oligoacenes: implication to molecular orientation at interfaces in organic FETs. *Mol. Cryst. Liq. Cryst.* **566**, 33–37 (2012).
61. Heeger, A. J., Kivelson, S., Schrieffer, J. R. & Su, W. P. Solitons in conducting polymers. *Rev. Mod. Phys.* **60**, 781–852 (1988).
62. Xu, Y. et al. Exploring the charge transport in conjugated polymers. *Adv. Mater.* **29**, 1702729 (2017).
63. Alberga, D. et al. Morphological and charge transport properties of amorphous and crystalline P3HT and PBTTT: insights from theory. *Phys. Chem. Chem. Phys.* **17**, 18742–18750 (2015).
64. Chaudhari, S. R. et al. Donor-acceptor stacking arrangements in bulk and thin-film high-mobility conjugated polymers characterized using molecular modelling and MAS and surface-enhanced solid-state NMR spectroscopy. *Chem. Sci.* **8**, 3126–3136 (2017).
65. Khim, D. et al. Precisely controlled ultrathin conjugated polymer films for large area transparent transistors and highly sensitive chemical sensors. *Adv. Mater.* **28**, 2752–2759 (2016).
66. Frisch, M. J. et al. *Gaussian 09, Rev. D. 01 and Gaussian 16, Rev A.03* (Gaussian, Inc.: Wallingford, CT, 2013 and 2016).

## Acknowledgements

The authors are grateful to Professor M. Matsushita and Professor K. Awaga for their help with the fabrication of parylene dielectric layers. This work was financially supported by a Grant-in-Aid for Scientific Research (A) (JP17H01069) and a Grant-in-Aid for Scientific Research on Innovative Areas (JP26102012) from the Japan Society for the Promotion of Science (JSPS) and by JST CREST (JPMJCR1715). This study was also supported by the 2018 Government-Funded Research Program of the Korea Institute of Machinery and Materials (NK210D).

## Author contributions

Y.Y.N. proposed the idea of applying FI-ESR methods on DA copolymers. W.-T.P. prepared the DA copolymers. H.T. designed the experiments, A.W. and M.K. carried out the FI-ESR experiments, device characteristics measurements, GIXD experiments, and AFM measurements on DA copolymers. S.K. carried out the FI-ESR experiments on PBTTT

device. Y.S. carried out the DFT calculations. S.-I.K. contributed to the discussion and interpretation of the data. H.T. wrote the manuscript with input from all co-authors. T.T. supervised the project. All authors discussed the results and approved the manuscript draft.

### Additional information

**Supplementary information** accompanies this paper at <https://doi.org/10.1038/s42005-019-0196-7>.

**Competing interests:** The authors declare no competing interests.

**Reprints and permission** information is available online at <http://npg.nature.com/reprintsandpermissions/>

**Publisher's note:** Springer Nature remains neutral with regard to jurisdictional claims in published maps and institutional affiliations.



**Open Access** This article is licensed under a Creative Commons Attribution 4.0 International License, which permits use, sharing, adaptation, distribution and reproduction in any medium or format, as long as you give appropriate credit to the original author(s) and the source, provide a link to the Creative Commons license, and indicate if changes were made. The images or other third party material in this article are included in the article's Creative Commons license, unless indicated otherwise in a credit line to the material. If material is not included in the article's Creative Commons license and your intended use is not permitted by statutory regulation or exceeds the permitted use, you will need to obtain permission directly from the copyright holder. To view a copy of this license, visit <http://creativecommons.org/licenses/by/4.0/>.

© The Author(s) 2019